nature nanotechnology

ARTICLES

https://doi.org/10.1038/s41565-020-00833-9

Graphene oxide membranes with stable porous structure for ultrafast water transport

Wen-Hai Zhang[1], Ming-Jie Yin[1], Qiang Zhao[2], Cheng-Gang Jin[1], Naixin Wang[1], Shulan Ji[1], Cody L. Ritt[3], Menachem Elimelech[3]✉ and Quan-Fu An[1]✉

The robustness of carbon nanomaterials and their potential for ultrahigh permeability has drawn substantial interest for separation processes. However, graphene oxide membranes (GOms) have demonstrated limited viability due to instabilities in their microstructure that lead to failure under cross-flow conditions and applied hydraulic pressure. Here we present a highly stable and ultrapermeable zeolitic imidazolate framework-8 (ZIF-8)-nanocrystal-hybridized GOm that is prepared by ice templating and subsequent in situ crystallization of ZIF-8 at the nanosheet edges. The selective growth of ZIF-8 in the microporous defects enlarges the interlayer spacings while also imparting mechanical integrity to the laminate framework, thus producing a stable microstructure capable of maintaining a water permeability of 60 l m^{-2} h^{-1} bar^{-1} (30-fold higher than GOm) for 180 h. Furthermore, the mitigation of microporous defects via ZIF-8 growth increased the permselectivity of methyl blue molecules sixfold. Low-field nuclear magnetic resonance was employed to characterize the porous structure of our membranes and confirm the tailored growth of ZIF-8. Our technique for tuning the membrane microstructure opens opportunities for developing next-generation nanofiltration membranes.

Global water scarcity is one of the greatest humanitarian crises of our time. The lack of adequate access to safe and clean drinking water already threatens the health of nearly two billion people and is only expected to worsen[1,2]. The dire need for increased water supply beyond what is available from the hydrologic cycle has necessitated advanced treatment processes to augment the water supply from unconventional sources, such as seawater, inland brackish water and various wastewaters. Membrane-based separations have attracted heightened interest for advanced treatment processes, largely due to their high efficacy and relatively low energy consumption.

Graphene oxide membranes (GOms) with multifunctional reactive groups and tunable microstructures have demonstrated great potential to realize ultrahigh water permeability, thus drawing substantial interest in recent years[3,4]. Furthermore, the interlayer spacing of laminate membranes can be easily adjusted to modulate the membrane permeability and selectivity; this has been proposed as a means to enable precise size-selective molecular sieving[5]. Although promising, the practical viability of GOms has been hindered by their inadequate water–solute selectivity and structural instability in aqueous solutions—both of which are highly influenced by the framework microstructure[6].

The imperfect stacking of graphene oxide (GO) laminates results in microporous defects (that is, framework defects) throughout the GOm that define its microstructure[6,7]. Recent work has shown that these microporous defects are the critical limiting factor in the achievable water–solute selectivity of GOms, and the influence of these defects depends on the extent to which they are filled[6]. Specifically, GOm microstructures with fewer or smaller voids produce more selective membranes. The loose microstructure of GOms also adversely affects the framework stability by promoting the delamination of GO nanosheets or the compaction of microscopic voids under typical operating conditions.

GOm instability is exacerbated under cross-flow conditions, which are typically employed in commercial pressure-driven membrane separation processes as they allow for continuous membrane separation with improved performance. Cross-flow operation exerts higher surface stress than the commonly studied bench-scale dead-end filtration mode and thus necessitates improved microstructure stability. As such, the loose GOm microstructures formed during traditional fabrication methods (for example, vacuum filtration, drop-casting, evaporation and dip-coating methods)[8] are insufficient. While some studies have addressed these issues[9–11], realizing selective and stable GO-based nanofiltration membranes remains highly challenging due to the lack of control over the GOm microstructures offered by traditional fabrication techniques. Therefore, novel fabrication approaches are needed to develop ultrapermeable GOms with high molecular selectivity that can endure long-term operation.

Here we report the design of highly stable and ultrapermeable laminate GO/zeolitic imidazolate framework-8 (ZIF-8) hybrid membrane architectures, where the confined growth of ZIF-8 in the microporous defects of a GOm stabilizes the framework microstructure and enables prolonged operation under cross-flow conditions and applied hydraulic pressure. We apply novel techniques to characterize the porous structure of our membrane architectures and elucidate the tailored growth of ZIF-8 nanocrystals. Finally, we assess the long-term stability of our membrane architectures and investigate the influence of ZIF-8 growth on their water and solute transport mechanisms. This study details the utility of novel techniques for improving the performance of GO-based membranes, providing insights into the design of next-generation nanofiltration membranes.

Membrane preparation

We prepared a ZIF-8-nanocrystal-hybridized frozen GOm (ZIF-8@f-GOm), in which the framework defects are filled and

[1]Beijing Key Laboratory for Green Catalysis and Separation, College of Environmental and Energy Engineering, Beijing University of Technology, Beijing, China. [2]Key Laboratory of Material Chemistry for Energy Conversion and Storage, Ministry of Education, School of Chemistry and Chemical Engineering, Huazhong University of Science and Technology, Wuhan, China. [3]Department of Chemical and Environmental Engineering, Yale University, New Haven, CT, USA. ✉e-mail: Menachem.elimelech@yale.edu; anqf@bjut.edu.cn

consequently stabilized in situ by ZIF-8 crystallization (Fig. 1a). This process differs considerably from previous studies that incorporate ZIF-8 into GO frameworks (Supplementary Table 1), resulting in the formation of selective nanochannels that allow rapid water transport over 180 h of operation without suffering from stability-related performance decline. Dispersed GO flakes (Supplementary Fig. 1) were filtered through a modified alumina tube membrane in a vacuum filtration cell (Supplementary Fig. 2), forming a continuous layer of wetted GO on the outer surface of the alumina tube. Afterwards, an ice-templating (IT) technique was employed to freeze dry the wetted GO framework (Methods), producing an f-GOm with enlarged interlayer spacings for reduced mass transport resistance to water[12]. Scanning electron microscopy (SEM) cross-sections depict an increase in the overall film thickness after IT (Fig. 1b,c), correlating to an increase in the interlayer spacing between the stacked nanosheets. However, without further modification, little mechanical support is available to prevent the collapse or delamination of the nanochannels and porous microstructure under typical filtration conditions.

Incorporating ZIF-8 supports into a nanoconfined framework has been challenging due to the lack of control over the ZIF-8 nanocrystal growth within the GOm framework. However, precise control over ZIF-8 growth can be obtained by moderating the balance between crystal nucleation and growth with the use of methanol (MeOH)/$NH_3{\cdot}H_2O$ (ref. [13]). To exploit this insight, we immersed the fabricated f-GOm in a solution of ZIF-8 precursors and subsequently treated it with MeOH/$NH_3{\cdot}H_2O$ mixed solution to selectively tailor the growth of ZIF-8 nanocrystals along the edges of the GO nanosheets (Supplementary Figs. 3 and 4).

Decorating the edges of the GO nanosheets with nanocrystals was intended to serve two purposes: (1) increase the mechanical integrity of the enlarged laminate structure to mitigate instability issues and (2) fill the framework defects to prevent the permeation of undesired solutes without hindering water permeation. ZIF-8 nanocrystals were specifically selected to achieve these goals due to their ability to crystallize in situ under mild conditions, their minimal frictional resistance towards water transport and their high water–solute selectivity. These characteristics are essential for achieving long-term stability while maintaining high separation performance[14]. The in situ growth of ZIF-8 nanocrystals resulted in a negligible change in the membrane thickness (Fig. 1d), suggesting that nanocrystal growth did not occur within the interlayer spacings and was confined to the framework defects.

The X-ray diffraction (XRD) data of the GO frameworks revealed a shift in the characteristic peak observed at 11.7° for our control GOm to 9.6° after freeze drying (Fig. 1e). This shift corroborates the observations from our SEM imaging and indicates that the IT technique increases the interlayer spacing from 0.75 nm (GOm) to 0.93 nm (f-GOm). Further, the XRD peak remains fixed at 9.6° after the ZIF-8 nanocrystals are incorporated into the f-GOm framework (Fig. 1e), suggesting that the membrane laminate structure is well preserved after ZIF-8 crystallization. The ZIF-8@f-GOm XRD peaks portray a superposition of the f-GOm and ZIF-8 characteristic peaks, thereby confirming the successful growth of ZIF-8 nanocrystals within the f-GOm framework[15].

A uniform distribution of ZIF-8 nanocrystals throughout ZIF-8@f-GOm, as seen from the Zn depth profile measured by X-ray photoelectron spectroscopy (Fig. 1f and Supplementary Fig. 5), indicates that the ZIF-8 precursor was able to fully penetrate the f-GOm framework. The electron diffraction data further corroborate this point, as the electron diffraction patterns of ZIF-8@f-GOm depict sharp spots that are absent from the patterns of GOm and f-GOm and contrast the circular patterns that coincide with the random orientation of the GO nanosheets (Fig. 1g)[16]. Linescans across the spots, illustrated as red arrows in Fig. 1g, show interplanar distances of 0.67 nm (1.5 nm^{-1}) that correspond to the <112> spacing for the ZIF-8 structure[16]. The Fourier transform infrared spectra of ZIF-8@f-GOm revealed bands (756 and 689 cm^{-1}) that are characteristic of the Zn–O and Zn–N vibrations found in ZIF-8, respectively (Supplementary Fig. 6), further confirming the in situ crystallization of ZIF-8 nanocrystals[17]. A reduction in the intensity of the 1,735 cm^{-1} band after the in situ crystallization of ZIF-8 in f-GOm stems from the coordination of carboxyl groups with Zn^{2+}. The carboxyl groups are only present along the periphery of the GO basal plane[18]; therefore, the carboxyl–Zn coordination indicates that the nucleation and growth of ZIF-8 is constrained only to the edges of the GO nanosheets. Additional evidence of edge-selective growth can be found in the Supporting Information (Supplementary Figs. 7 and 8 and Supplementary Table 2). The carboxyl–Zn coordination also signifies that ZIF-8 is covalently bound within ZIF-8@f-GOm rather than weakly adsorbed[19]. The properties of isolated ZIF-8 nanocrystals are provided in Supplementary Fig. 9.

Characterization of porous framework

Brunauer–Emmett–Teller surface area analysis was conducted to characterize the porous structure of our GO-based membranes. Both GOm and f-GOm displayed negligible N_2 adsorption, whereas ZIF-8@f-GOm adsorbed ~80 $cm^3\,N_2\,g^{-1}$, corresponding to a specific surface area of 226.6 $m^2\,g^{-1}$ (Fig. 2a). Such a disparity in N_2 adsorption can be attributed to the inaccessibility of N_2 within the interlayer free spacing (that is, the unoccupied space between the neighbouring sheets) of the GO nanosheets. As a result, we employed CO_2 as a probe molecule to measure the porous volume throughout the GO laminates, as CO_2 has been found to permeate through GOms at a 20-fold higher rate than N_2 due to its enhanced chemical affinity[20].

Figure 2b shows a sixfold increase in the CO_2 adsorption volume of f-GOm (41.93 $cm^3\,g^{-1}$) compared with GOm (6.47 $cm^3\,g^{-1}$), which is in agreement with the increase in the overall porous structure after freeze drying. Although the growth of ZIF-8 nanocrystals in f-GOm did not reduce the interlayer spacing of the membrane, it decreased the total CO_2 adsorption with respect to the membrane mass. Due to the inability of ZIF-8 to grow within the nanochannels, this decline in porosity can be attributed to the filling of the microporous defects by ZIF-8. The pore size distributions of our GO frameworks also reflect an increase in the membrane porosity after freeze drying and subsequent decrease after ZIF-8 growth (Fig. 2c).

Notably, 0.37 nm pores appear after freeze drying the GOm. We believe that this pore regime is an artefact of the structural heterogeneity of the GOms. Structural heterogeneity—induced by the non-uniform stacking of GO nanosheets—may result in sections of GO nanochannels that are smaller than the average interlayer free spacing, thus prohibiting CO_2 adsorption. However, previous simulation studies have shown that the swelling of the heterogeneous laminates can sufficiently enlarge these spaces for gas molecules to penetrate and are in good agreement with our experimental results[21]. These pores are probably located near the intersection of the GO edges with the neighbouring GO sheets, where the non-uniform stacking occurs[21]. Therefore, the selective growth of ZIF-8 nanocrystals at the nanosheet edges could explain the decrease in the density of the 0.37 nm pores.

Low-field nuclear magnetic resonance (LF-NMR) was employed to study the molecular dynamics of the solvents confined within the porous matrices. This method applies multi-pulse sequences to protons, namely, Carr–Purcell–Meiboom–Gill, to measure the transverse relaxation time (T_2) of the liquid molecules inside the pore and offers information regarding the void size—or degree of solvent confinement—within the membrane[22].

Membrane pores were probed with MeOH, the solvent used for ZIF-8 precursors (Fig. 2d). The T_2 for all the GO-based membranes possess a broad population in the time domain of 10^3–10^4 ms (Fig. 2d), indicative of the free MeOH molecules existing around

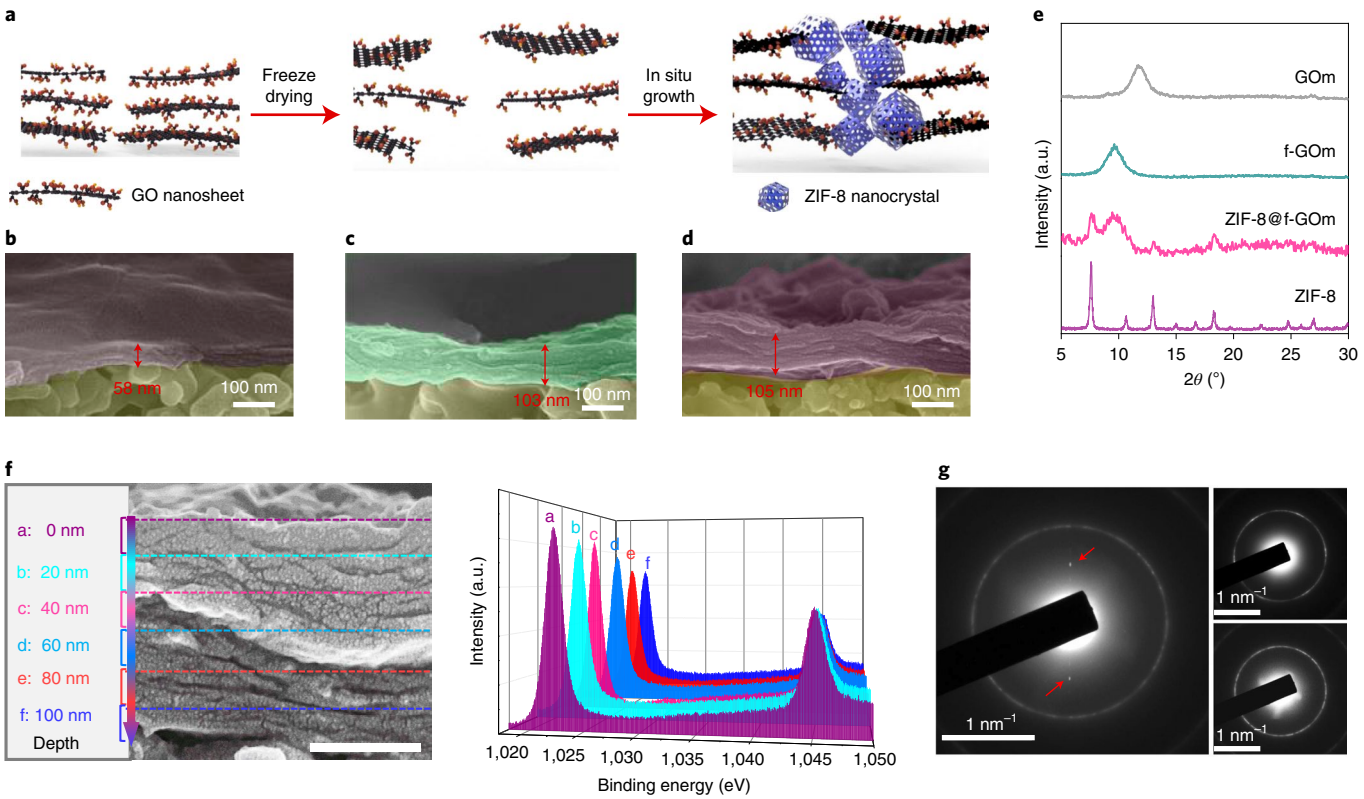

Fig. 1 | Preparation and characterization of ZIF-8@f-GOm. a, Schematic of ZIF-8@f-GOm preparation, in which the GO framework is freeze dried by the IT technique before subsequently growing ZIF-8 nanocrystals in the microporous defects to act as mechanical supports. **b**–**d**, SEM cross-sectional images of GOm (**b**), f-GOm (**c**) and ZIF-8@f-GOm (**d**). **e**, XRD patterns of GOm, f-GOm, ZIF-8@f-GOm and ZIF-8. a.u., arbitrary units. **f**, Magnified SEM image of ZIF-8@f-GOm (left) and the high-resolution Zn X-ray photoelectron spectroscopy data corresponding to the different sample depths across ZIF-8@f-GOm (right). Scale bar, 50 nm. **g**, Electron diffraction pattern of GOm (top right), f-GOm (bottom right) and ZIF-8@f-GOm (left). The red arrows indicate two sharp spots observed in the diffraction pattern where the linescans were taken.

the membrane (that is, free space). For GOm, only a single population exists in the nanoconfinement domain (that is, time domain of 10–400 ms). This nanoconfined population represents MeOH located in the microporous defects. Freeze drying leads to an increase in the relaxation time of the nanoconfined population, coinciding with the increase in the f-GOm microporous defects. Further, the LF-NMR data of f-GOm show the appearance of an additional population in the nanoconfinement domain, located at lower relaxation times (~20 to 80 ms). This new population of smaller pores probably correlates with vacancies created around the ordered edges of the interlayer spacings. An upward shift in the relaxation time as well as an increase in the overall signal intensity from GOm to f-GOm further corroborates an increase in the quantity and size of the microporous defects after freeze drying. Additionally, the absence of a signal from the sub-nanometre confinement region (that is, time domain of 0–10 ms) verifies that the MeOH molecules are unable to penetrate between the laminated GO nanosheets. Consequently, ZIF-8 growth is constrained to the porous defects of f-GOm (Fig. 2e).

Long-term stability and selectivity

The role of the ZIF-8 nanocrystals in improving the selectivity and long-term stability of GO frameworks for nanofiltration was studied under cross-flow conditions and applied hydraulic pressure (Supplementary Fig. 10). The results provided here are based on ZIF-8@f-GOm prepared under optimized conditions (for example, GO concentration, filtration time and ZIF-8 crystallization process), as shown in Supplementary Figs. 11–14. Over 180 h of continuous operation, the water permeability of f-GOm and GOm decreased by 50% and 80%, respectively (Fig. 3a,b). By contrast, the ultrahigh permeability of ZIF-8@f-GOm remained largely stable over the same duration, decreasing by only 8%. Furthermore, the steady-state water permeance of ZIF-8@f-GOm is roughly 1.5- and 30-fold greater than that of f-GOm and GOm, respectively. In addition to ultrahigh permeability, ZIF-8@f-GOm fully excluded methylene blue (MB), a common dye molecule, while GOm and f-GOm showed only 98% and 94% MB rejection, respectively (Fig. 3c). Collectively, ZIF-8@f-GOm highlights substantial improvements in the water permeability, selectivity and performance stability over f-GOm and GOm.

This is one of the first studies to demonstrate novel fabrication techniques for improving the long-term operational stability of GO-based membranes while also mitigating the adverse effects of microporous defects on water–solute selectivity. Moreover, we stress that nanofiltration processes are operated under continuous cross-flow conditions and applied hydraulic pressure, where the stability of the membrane microstructure is challenged by hydrodynamic surface shearing and compaction. As such, the performance of ZIF-8@f-GOm was compared with other GO-based membranes under cross-flow conditions as reported in the literature (Fig. 3d and Supplementary Table 3)[23–28]. Notably, in comparison, ZIF-8@f-GOm exhibits the highest water permeance ($49.8\,l\,m^{-2}\,h^{-1}\,bar^{-1}$) coupled with near-perfect MB rejection (~100%).

To further investigate the stability of the ZIF-8@f-GOm microstructure, we increased the applied transmembrane pressure to 7 bar (Fig. 3e). The water flux of GOm and ZIF-8@f-GOm linearly increased up to 7 bar, indicating no pressure-induced failure or compaction of the membrane microstructure[29]. In contrast, the

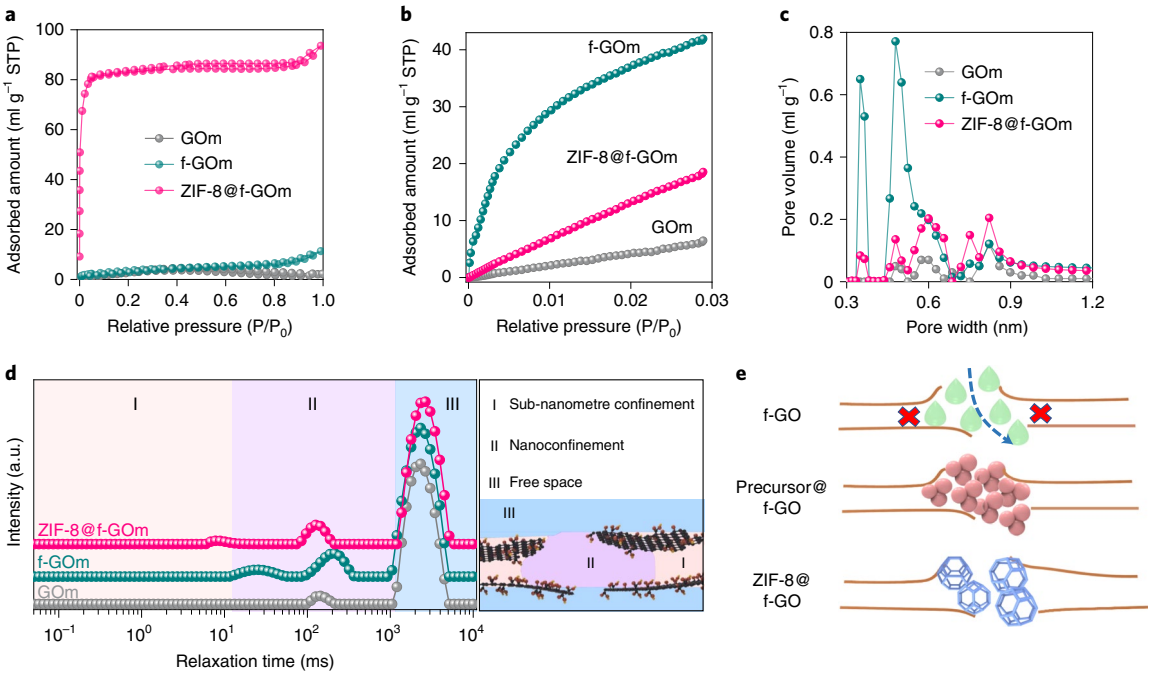

Fig. 2 | Pore structure of GO-based membranes and elucidation of ZIF-8 growth mechanisms. a,**b**, Brunauer–Emmett–Teller adsorption isotherms, measured at standard temperature and pressure (STP, 273 K and 101.325 kPa, respectively), of GOm, f-GOm and ZIF-8@f-GOm with N_2 (**a**) and CO_2 (**b**) as the probe molecules. **c**, Pore size distribution of GOm, f-GOm and ZIF-8@f-GOm probed by CO_2 molecules. **d**, ^{1}H time-domain nuclear magnetic resonance spectra of GOm and f-GOm with MeOH as the probe molecule. a.u., arbitrary units. **e**, Schematic of our strategy to precisely position ZIF-8 nanoparticles at the edges of the GO nanochannels. First, the f-GOm is immersed in mixed MeOH precursor solution (green drops) that cannot penetrate between the GO nanosheets (top). After the precursors coordinate with the carboxyl groups located at the edge of the GO nanosheets, crystal nucleation begins (red orbs). Lastly, crystal growth continues until ZIF-8 nanocrystals (blue cages) fill the microporous voids.

water flux of f-GOm decayed with respect to pressure until reaching an inflection point at 5 bar, where the water flux then linearly increased. This phenomenon is the result of the gradual compaction of the enlarged f-GOm microporous structure at increased hydraulic pressures, and the inflection is the point at which the f-GOm microstructure reached its maximum compaction. The absence of compaction in ZIF-8@f-GOm at elevated hydraulic pressure demonstrates the improved mechanical integrity of the enlarged microporous structure, owing to the rigidity of the supporting ZIF-8 nanocrystals.

It has been previously shown that ZIF-8 is unstable in water when its weight fraction is below 0.06%—a consequence of hydrolosis[30,31]. We found no evidence of ZIF-8 dissolution when measuring the ion conductivity of the feed and permeate solutions after circulating deionized water, which had been equilibrated with ambient CO_2 to ensure there was no change in the conductivity due to CO_2 adsorption, for 180 h. This was corroborated by the XRD data (Supplementary Fig. 15), which showed no noticeable change in the crystal structure of ZIF-8@f-GOm after immersion in deionized water for seven days. The water stability of the ZIF-8 nanocrystals may be attributed to the in situ growth of ZIF-8 within the confined f-GOm framework, where the top GO layer may act as a protective barrier that prevents the erosion of ZIF-8 nanocrystals under the cross-flow conditions.

Transport mechanisms

The LF-NMR data of water dynamics throughout the GO-based membranes indicate the same confinement behaviour in the microporous structure (that is, time domain of 10–400 ms) that was observed by the LF-NMR data with MeOH (Fig. 4a). However, when using water as the probe molecule, a population in the sub-nanometre confinement region (that is, time domain of 0–10 ms) appeared for all the membrane architectures. A population within the sub-nanometre confinement region is indicative of water molecules penetrating the interlayer spacings of GO nanosheets. Notably, the relaxation time of the sub-nanometre-confined water shifts from 0.5 to 2.5 ms after freeze drying and remains at 2.5 ms after ZIF-8 growth. Combined with the XRD data of the wetted frameworks (Supplementary Fig. 15), it is clear that the increase in the sub-nanometre relaxation time of f-GOm is a consequence of the interlayer expansion after freeze drying. ZIF-8@f-GOm does not experience further swelling, probably due to the embedded ZIF-8 nanocrystals holding the framework intact. The agreement between the XRD and LF-NMR characterization data indicates that LF-NMR is not only useful for characterizing the membrane microstructure but is also valid for characterizing the membrane nanostructure (that is, interlayer spacings).

The ability of ZIF-8@f-GOm to fully exclude MB, while still allowing water molecules to pass through the ZIF-8-filled microporous defects at a high rate, indicates that ZIF-8 nanocrystals act as selective filters for large organic molecules (Fig. 4b). This can be observed by the >30-fold increase in water–MB permselectivity of ZIF-8@f-GOm compared with f-GOm (Supplementary Table 4). Notably, the growth of hydrophobic ZIF-8 nanocrystals within the microporous structure was associated with decreased hydrophobicity (that is, decreased water contact angle) and promoted a more rapid penetration of water molecules into ZIF-8@f-GOm (2.3 s) than the other GO-based membranes (Fig. 4c). Anomalous increases in membrane hydrophilicity after the incorporation of hydrophobic ZIF-8 nanocrystals have been previously observed[32]. We surmise that this abnormal phenomenon may be the result of a reduction in the effective defect pore size upon ZIF-8 growth, which could enhance capillary forces and promote water sorption[33].

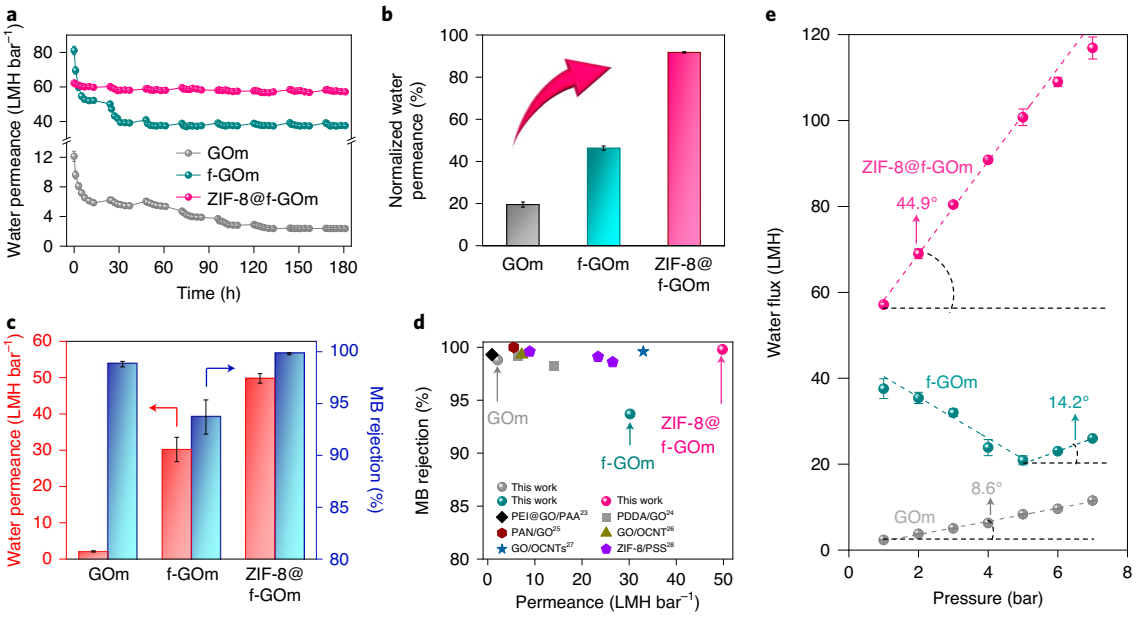

Fig. 3 | Nanofiltration performance of GO-based membranes under cross-flow conditions. a,**b**, Long-term stability of GO-based membrane permeance conducted under cross-flow conditions with an applied transmembrane pressure of 1 bar. Pure water permeance (in l m^{-2} h^{-1} bar^{-1}, LMH bar^{-1}) of GOm, f-GOm and ZIF-8@f-GOm over a 180 h operating period (**a**) and normalized water permeance after reaching equilibrium (**b**). **c**, Water permeance and MB rejection for GO-based membranes. Measurements were taken at an MB feed concentration of 100 ppm and a transmembrane pressure of 1 bar. The red and blue arrows represent data corresponding to water permeance and MB rejection, respectively. **d**, Comparison of MB rejection and water permeance for GO-based membranes reported in the literature with the GO-based membranes used in this work. Data were included from measurements taken under cross-flow conditions found in Supplementary Table 3 (refs. [23–28]). **e**, Relation between water flux and operating pressure for GOm, f-GOm and ZIF-8@f-GOm. Water fluxes were recorded after membranes were maintained under steady-state operation for at least 24 h. The angles shown in **e** reflect the slope of the curves, which indicates relative differences in membrane permeance after compaction. Error bars in **b**, **c** and **e** represent the standard deviation from triplicate experiments.

Zeta potentials of our GO-based membranes were quantified to assess the potential influence of charge-based exclusion (that is, Donnan exclusion) on the selectivity of charged organic molecules, such as MB (Fig. 4d). The dissociation of oxygen-containing functional groups (for example, carboxylic acid groups) decorated across the GO nanosheets are responsible for their intrinsic negative charge[18]. Although the zeta potential remains unchanged after freeze drying, the growth of ZIF-8 nanocrystals decreases the zeta potential of ZIF-8@f-GOm by approximately half. This observation is attributable to the coordination of ZIF-8 with carboxyl groups, thus reducing the free carboxyl content across the membrane. Although the reduced carboxyl density may mitigate Donnan exclusion by ZIF-8@f-GOm, the enhanced rejection of negatively charged MB by ZIF-8@f-GOm indicates that ZIF-8 nanocrystals also act as steric filters (Fig. 3c).

Neutral organic molecules of varying molecular weights were used to estimate the molecular weight cut-off (MWCO) and assess the steric exclusion of our GO-based membranes (Fig. 4e). MWCO refers to the lowest molecular weight solute in which 90% of the solute is retained by the membrane—approximately 1.3 kDa for ZIF-8@f-GOm; this MWCO approximately correlates to an average pore size of ~1 nm (ref. [34]). A comparison with the MWCO of other membranes is provided in Supplementary Table 5. Steric hindrance imposed upon solute transport is reduced after freeze drying and then subsequently increased after ZIF-8 growth due to the change in the free space of the microporous defects (Fig. 4e). While the reduced MWCO illustrates that ZIF-8 can successfully fill the free space of the defect, it is still larger than the typical pore size within the ZIF-8 nanocrystals. This suggests that microporous defects may not be completely filled during crystal growth. Further, we find the MWCO of ZIF-8@f-GOm to be substantially larger than the size of MB (molecular weight ≈ 800 Da), which was nearly fully excluded (Fig. 3c). This observation indicates that Donnan exclusion plays a prominent role in the rejection of charged solutes by ZIF-8@f-GOm. Further assessment of negatively charged solute rejection (Supplementary Fig. 16) demonstrates that Donnan exclusion enables ZIF-8@f-GOm to achieve ≥90% rejection of organic molecules as small as 327 Da (for example, methyl orange). We have also examined the role of Donnan exclusion in desalination, where the negatively charged carboxylate groups enable salt (ion) rejection comparable to nanofiltration (discussion in Supplementary Information and Supplementary Fig. 17).

Conclusion

We successfully fabricated a highly stable ZIF-8@f-GOm possessing ultrahigh permeability (~60 l m^{-2} h^{-1} bar^{-1}) with improved solute selectivity (MWCO ≈ 1.3 kDa). This novel GOm architecture was achieved by modifying a standard GOm with an IT technique followed by the in situ crystallization of ZIF-8. By controlling the freeze-drying conditions, we were able to precisely tailor the ZIF-8 nanocrystals within the porous defects. The influence of ZIF-8 nanocrystals in the microporous defects was twofold: improved framework stability and selective water–solute separation. Mechanical support imparted by the covalently bound ZIF-8 nanocrystals prevented the compaction of the microporous voids, giving rise to long-term stability in ZIF-8@f-GOm, whereas the steric resistance imposed by ZIF-8 to organic molecules resulted in highly selective membranes. Notably, this study marks the first attempt to precisely fill the microporous defects of GO-based membranes to improve the selectivity while maintaining ultrahigh permeability for an extended duration (180 h). This work demonstrates that innovative fabrication techniques can help overcome limitations

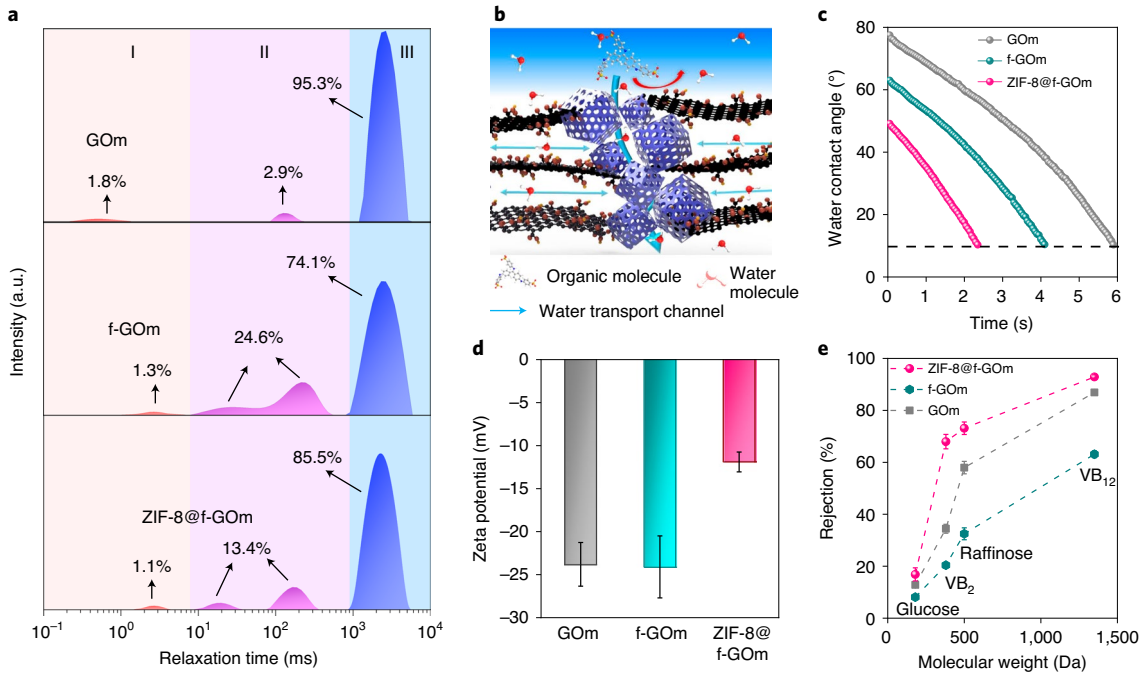

Fig. 4 | Elucidation of ZIF-8@f-GOm separation mechanisms. a, ^{1}H time-domain nuclear magnetic resonance spectra of GOm, f-GOm and ZIF-8@f-GOm. LF-NMR experiments were conducted with water as the probe molecule. a.u., arbitrary units. **b**, Illustration of the ZIF-8@f-GOm separation mechanism and water transport across the membrane, where water is allowed to be transported between the interlayer spacings and through the ZIF-8-filled microporous defects (blue arrows). In contrast, large organic molecules are excluded (red arrow) from the microporous defects by the sterically selective ZIF-8 nanocrystals (blue cubes). **c**, Dynamic water contact angle of GOm, f-GOm and ZIF-8@f-GOm surfaces, where decreased water contact angles correspond to increased hydrophilicity at the membrane surface. **d**, Approximations of GO-based membrane surface charge by zeta potential via streaming potential measurements. **e**, Separation of neutral-charge organic molecules by GOm, f-GOm and ZIF-8@f-GOm. Error bars in **d** and **e** represent the standard deviation from triplicate experiments.

associated with the loose microstructure of GO-based membranes, opening the door to the design of high-efficacy nanofiltration membranes based on novel two-dimensional materials.

Online content

Any methods, additional references, Nature Research reporting summaries, source data, extended data, supplementary information, acknowledgements, peer review information; details of author contributions and competing interests; and statements of data and code availability are available at https://doi.org/10.1038/s41565-020-00833-9.

Received: 26 February 2020; Accepted: 2 December 2020;
Published online: 21 January 2021

References

1. Elimelech, M. & Phillip, W. A. The future of seawater desalination: energy, technology, and the environment. *Science* **333**, 712–717 (2011).
2. Baird R. B., Eaton A. D. & Rice E. W. (eds) *Standard Methods for the Examination of Water and Wastewater*, 23rd edn (American Water Works Association, 2017).
3. Perreault, F., de Faria, A. F., Nejati, S. & Elimelech, M. Antimicrobial properties of graphene oxide nanosheets: why size matters. *ACS Nano* **9**, 7226–7236 (2015).
4. Liu, G. P., Jin, W. Q. & Xu, N. P. Graphene-based membranes. *Chem. Soc. Rev.* **44**, 5016–5030 (2015).
5. Joshi, R. K. et al. Precise and ultrafast molecular sieving through graphene oxide membranes. *Science* **343**, 752–754 (2014).
6. Ritt, C. L., Werber, J. R., Deshmukh, A. & Elimelech, M. Monte Carlo simulations of framework defects in layered two-dimensional nanomaterial desalination membranes: implications for permeability and selectivity. *Environ. Sci. Technol.* **53**, 6214–6224 (2019).
7. Yang, Q. et al. Ultrathin graphene-based membrane with precise molecular sieving and ultrafast solvent permeation. *Nat. Mater.* **16**, 1198–1202 (2017).
8. Ma, J. X., Ping, D. & Dong, X. F. Recent developments of graphene oxide-based membranes: a review. *Membranes* **7**, 52 (2017).
9. Wei, Y. et al. Declining flux and narrowing nanochannels under wrinkles of compacted graphene oxide nanofiltration membranes. *Carbon* **108**, 568–575 (2016).
10. Chong, J. Y., Wang, B., Mattevi, C. & Li, K. Dynamic microstructure of graphene oxide membranes and the permeation flux. *J. Membr. Sci.* **549**, 385–392 (2018).
11. Saraswat, V. et al. Invariance of water permeance through size-differentiated graphene oxide laminates. *ACS Nano* **12**, 7855–7865 (2018).
12. Deville, S., Saiz, E., Nalla, R. K. & Tomsia, A. P. Freezing as a path to build complex composites. *Science* **311**, 515–518 (2006).
13. Shen, K. et al. Ordered macro-microporous metal–organic framework single crystals. *Science* **359**, 206–210 (2018).
14. Li, X. et al. Metal–organic frameworks based membranes for liquid separation. *Chem. Soc. Rev.* **46**, 7124–7144 (2017).
15. Huang, A. S., Liu, Q., Wang, N. Y., Zhu, Y. Q. & Caro, J. Bicontinuous zeolitic imidazolate framework ZIF-8@GO membrane with enhanced hydrogen selectivity. *J. Am. Chem. Soc.* **136**, 14686–14689 (2014).
16. Ma, X. L. et al. Zeolitic imidazolate framework membranes made by ligand-induced permselectivation. *Science* **361**, 1008–1011 (2018).
17. Bustamante, E. L., Fernandez, J. L. & Zamaro, J. M. Influence of the solvent in the synthesis of zeolitic imidazolate framework-8 (ZIF-8) nanocrystals at room temperature. *J. Colloid Interf. Sci.* **424**, 37–43 (2014).
18. Dreyer, D. R., Park, S., Bielawski, C. W. & Ruoff, R. S. The chemistry of graphene oxide. *Chem. Soc. Rev.* **39**, 228–240 (2010).
19. Yang, H. Y. et al. Vacuum-assisted assembly of ZIF-8@GO composite membranes on ceramic tube with enhanced organic solvent nanofiltration performance. *J. Membr. Sci.* **545**, 158–166 (2018).
20. Kim, H. W. et al. Selective gas transport through few-layered graphene and graphene oxide membranes. *Science* **342**, 91–95 (2013).
21. Williams, C. D., Carbone, P. & Siperstein, F. R. Computational characterisation of dried and hydrated graphene oxide membranes. *Nanoscale* **10**, 1946–1956 (2018).
22. Hu, M. M. et al. Surface functional groups and interlayer water determine the electrochemical capacitance of $Ti_3C_2T_x$ MXene. *ACS Nano* **12**, 3578–3586 (2018).

23. Wang, N. X., Ji, S. L., Zhang, G. J., Li, J. & Wang, L. Self-assembly of graphene oxide and polyelectrolyte complex nanohybrid membranes for nanofiltration and pervaporation. *Chem. Eng. J.* **213**, 318–329 (2012).
24. Wang, L. et al. Layer-by-layer self-assembly of polycation/GO nanofiltration membrane with enhanced stability and fouling resistance. *Sep. Purif. Technol.* **160**, 123–131 (2016).
25. Qiu, Z. Y., Ji, X. F. & He, C. J. Fabrication of a loose nanofiltration candidate from polyacrylonitrile/graphene oxide hybrid membrane via thermally induced phase separation. *J. Hazard. Mater.* **360**, 122–131 (2018).
26. Kang, H. et al. Sandwich morphology and superior dye-removal performances for nanofiltration membranes self-assemblied via graphene oxide and carbon nanotubes. *Appl. Surf. Sci.* **428**, 990–999 (2018).
27. Yang, L. B., Wang, Z. & Zhang, J. L. Zeolite imidazolate framework hybrid nanofiltration (NF) membranes with enhanced permselectivity for dye removal. *J. Membr. Sci.* **532**, 76–86 (2017).
28. Zhang, R. et al. Coordination-driven in situ self-assembly strategy for the preparation of metal–organic framework hybrid membranes. *Angew. Chem. Int. Ed.* **53**, 9775–9779 (2014).
29. Wang, Y. J. et al. Water transport with ultralow friction through partially exfoliated g-C_3N_4 nanosheet membranes with self-supporting spacers. *Angew. Chem. Int. Ed.* **56**, 8974–8980 (2017).
30. Duan, J. T. et al. High-performance polyamide thin-film-nanocomposite reverse osmosis membranes containing hydrophobic zeolitic imidazolate framework-8. *J. Membr. Sci.* **476**, 303–310 (2015).
31. Liu, X. et al. Improvement of hydrothermal stability of zeolitic imidazolate frameworks. *Chem. Commun.* **49**, 9140–9142 (2013).
32. Zhang, H., Liu, D., Yao, Y., Zhang, B. & Lin, Y. S. Stability of ZIF-8 membranes and crystalline powders in water at room temperature. *J. Membr. Sci.* **485**, 103–111 (2015).
33. Wu, L. et al. Highly efficient three-dimensional solar evaporator for high salinity desalination by localized crystallization. *Nat. Comm.* **11**, 521 (2020).
34. Wilkinson K. J. & Lead J. R. (eds) *Environmental Colloids and Particles: Behaviour, Separation and Characterisation* (John Wiley & Sons, 2007).

Methods

Materials. GO (diameter > 500 nm) was obtained from Nanjing XFNANO Materials Tech. 2-Methylimidazole was purchased from Aldrich. $Zn(NO_3)_2{\cdot}6H_2O$ was provided by Shanghai Titan Scientific. Dopamine was obtained from Ark Pharm. Tris(hydroxymethyl) aminomethane was provided by Adamas Reagent. MeOH, Eriochrome Black T, methyl orange, Congo red, Evans blue, MB, glucose, raffinose, tetracycline, vitamin B_2 and vitamin B_{12} (VB_{12}) were purchased from the Beijing Chemical Factory. All the chemicals were used as received without further purification. Further, 50-mm-long tubular ceramic substrates with inner and outer diameters of 8.5 and 13.5 mm, respectively, were supplied by JieXi LiShun Technology. The tubular ceramic substrate is composed of a support layer and a dense layer. The thickness of the dense layer is approximately 5 µm. The pore size is approximately 100 nm.

Preparation of GO and f-GO membranes. GO powder was dispersed in deionized water, as shown in Supplementary Fig. 1a, and it was ultrasonicated several times to exfoliate bulk GO into GO nanosheets. The as-prepared GO solution was then poured onto PDA-modified ceramic tubes under a pressure of 500 Pa (Supplementary Fig. 2). After several minutes, wet GOms on ceramic tubes were obtained and treated under two separate, controlled conditions: (1) dried at 60 °C in an oven, referred to as GOm; (2) freeze dried via the IT technique, referred to as f-GOm.

Preparation of ZIF-8@GO and ZIF-8@f-GO membranes. ZIF-8@f-GO membrane was prepared by in situ nano-casting. First, 8.15 g of $Zn(NO_3)_2{\cdot}6H_2O$ and 6.75 g of 2-methylimidazole were dissolved in MeOH to prepare the ZIF-8 precursor solution (Supplementary Fig. 4a). Then the f-GO membrane was immersed in the precursor solution for 3 h and vacuum degassed for 10 min to ensure all the microporous defects were filled with the precursor solution. The impregnated composite membrane was dried at 50 °C in an oven for several hours. The obtained membrane (denoted as precursor@f-GO) was soaked with a $CH_3OH/NH_3{\cdot}H_2O$ (v/v, named as x:y) mixed solution at room temperature for 12 h. Finally, the resulting composite membrane was dried at 50 °C for 12 h to form ZIF-8@f-GOm.

Analytical methods. *Morphology characterization.* SEM images were taken with an FEI Helios Nano-lab 600i FIB/SEM DualBeam system. The same microscope was used to prepare the cross-sectional transmission electron microscopy samples. High-resolution transmission electron microscopy images were acquired using an FEI Titan ETEM microscope operated at 300 kV. The surface roughness of the composite membranes was observed by atomic force microscopy (Dimension Icon, Bruker).

Pore structure characterization. Brunauer–Emmett–Teller surface area and pore size measurements were performed with N_2 adsorption/desorption isotherms at 77 K on a Micromeritics ASAP 2020M instrument. Before the measurements, the samples were degassed at 100 °C for 12 h. The pore size distributions were evaluated by using the Dubinin–Astakhov method for micropores with the CO_2 adsorption data and assuming a slit pore model. An NMI20 NMR analyser (Suzhou NIUMAG Analysis Instruments Corporation) was used to measure the T_2 values at 20 MHz. The magnet temperature was set at 32 °C to ensure a constant rate of molecular motion for probing the system.

Surface properties' characterization. Dynamic contact angles of the membranes were determined by the sessile drop method using OCAH 200, a contact angle goniometer. The measurements were done using 1 µl of water as the probe liquid, and the average value from five random locations was used as the contact angle to minimize experimental errors. Zeta potentials of the membrane surface were calculated via streaming potential measurements by an electrokinetic analyser (Anton Paar, SurPASS), where 0.83 mmol l^{-1} of KCl solution was passed over the membrane surface under a pressure of 0.03 MPa.

Other characterizations. Powder X-ray diffraction patterns were recorded in the 2θ (that is, the diffraction angle between the incident X-ray and the diffraction line) range of 5–30° at room temperature using a D8 ADVANCE (Bruker AXS) in transmission geometry using Cu Kα radiation (15 mA and 40 kV) at a scan rate of 2° min^{-1} and a step size of 0.02°. An attenuated total reflectance Fourier transform infrared spectrometer (VERTEX 70, Bruker) and X-ray photoelectron spectroscope (ESCALAB 250XL, Thermo Scientific) were used to confirm the reactions during the membrane preparation process.

Membrane performance. All the pure water permeability (that is, water permeance) and organic molecule separation measurements were conducted in a cross-flow nanofiltration system. The effective membrane area was 10 cm^2. The measurements were conducted under applied pressures varying from 1 to 7 bar at room temperature with a cross-flow velocity of ~31 cm s^{-1}. All the separation performance and water flux data, excluding the dynamic tests, were recorded after the performance of the fabricated membranes reached the steady state. The time to reach the steady state depended on the membrane architecture and the applied pressure, varying from several hours to several days.

Data availability

The data that support the plots within this paper and other findings of this study are available from the corresponding authors upon reasonable request.

Acknowledgements

This work is financially supported by the National Natural Science Foundation of China (21878004 and 21576003), the Importation and Development of High-Caliber Talents Project of Beijing Municipal Institutions (CIT&TCD20170305), Beijing Municipal Natural Science Foundation co-sponsored by Beijing Natural Science Foundation Committee and Beijing Education Committee (KZ201910005001) and National Key R&D Program of China (2019YFC1806000). We also acknowledge the United States National Science Foundation Graduate Research Fellowship awarded to C.L.R. (DGE1752134).

Author contributions

W.-H.Z., C.L.R., M.E. and Q.-F.A. conceived and designed the experiments. M.E. and Q.-F.A. supervised the study and experiments. W.-H.Z. and C.-G.J. conducted the membrane fabrication, characterization and performance tests. S.J. and Q.-F.A. supported all the characterizations. W.-H.Z., M.-J.Y., N.W., C.L.R. and Q.-F.A. analysed the experimental results. W.-H.Z., M.-J.Y. and Q.Z. wrote the paper. C.L.R., M.E. and Q.-F.A. revised the manuscript. All the authors discussed the results and provided comments.

Competing interests

The authors declare no competing interests.

Additional information

Supplementary information is available for this paper at https://doi.org/10.1038/s41565-020-00833-9.

Correspondence and requests for materials should be addressed to M.E. or Q.-F.A.

Peer review information *Nature Nanotechnology* thanks Ho Bum Park and the other, anonymous, reviewer(s) for their contribution to the peer review of this work.